Dynamics and scaling laws of underwater granular collapse with varying aspect ratios

L. Jing,[1] G. C. Yang,[1] C. Y. Kwok,[1,*] and Y. D. Sobral[2]
[1]*Department of Civil Engineering, The University of Hong Kong, Pokfulam Road, Hong Kong*
[2]*Departamento de Matemática, Universidade de Brasília, Campus Universitário Darcy Ribeiro, 70910-900 Brasília, DF, Brazil*

(Received 20 June 2018; published 9 October 2018)

We perform coupled fluid-particle simulations to understand the granular collapse in an ambient fluid (in particular, water) with a wide range of initial aspect ratios. We observe both similar and distinct features in underwater collapses compared to their dry counterparts. As aspect ratio a increases, the normalized runout distance follows a piecewise power-law growth, transitioning at $a = 2.5$. We associate this transition with the different growth rates of kinetic energy (with a) in vertical and horizontal directions. The ability of utilizing available energy for horizontal motion becomes limited when $a > 2.5$. Moreover, the front propagation during underwater collapses can be well scaled by using the initial column height as length scale and considering a reduced gravity (due to buoyancy) in timescale. Under the reduced gravity, the initial fall of tall columns is found to be ballistic, consistent with dry collapses. On the other hand, underwater collapses (especially for large a) exhibit unique dynamics due to the presence of water. The eddies generated in water, which may carry considerable fluid inertia, tend to erode the surface of the granular layer, thus modifying the deposit morphology. The energy conversion is also affected by the ambient fluid. While water obviously consumes energy from the granular phase through fluid-particle interactions, it actually increases the efficiency of energy conversion from vertical to horizontal directions. The latter effect compensates the difference of runout distance between underwater and dry collapses.

DOI: 10.1103/PhysRevE.98.042901

I. INTRODUCTION

The collapse of granular columns on a horizontal plane is a popular model case for understanding granular flows, which attracts attention from theoretical, experimental, and numerical research communities, fascinated by the rich flow behaviors it exhibits [1]. The granular collapse problem is relevant to the transport of granular products in agricultural, chemical, pharmaceutical, and other industrial applications. It also has a direct relevance to geophysical situations, such as the risk assessment of debris flows, rock avalanches, and submarine landslides [2,3]. Its basic configuration can be adapted to study granular avalanches on inclines [4,5] and the segregative behaviors of multidisperse materials [6].

Dry granular collapses, in which the influence of interstitial and ambient fluids is negligible, have been extensively studied over the last two decades. Laboratory experiments have identified the initial (height to length) aspect ratio as a primary factor and revealed simple yet important power-law relations between runout distance and aspect ratio [4,7–11]. The role of other factors, such as the initial mass, particle size, and base roughness, were found to be minor [8,10]. Alternatively, particle-based numerical simulations have been used to reproduce the experimental observations and to add insights by studying energy dissipations [12,13], the role of particle properties [14,15], and the validity of granular constitutive models [16]. From the theoretical point of view, attempts have been made to apply thin-layer continuum models to this problem [17,18], with particular attention on the treatment of vertical inertia in the collapse of tall columns [19,20]. Non-thin-layer continuum models that involve a specific scheme for free-surface tracking are alternatives for the continuum modeling of granular collapses [21–25]. One of the remaining challenges is to provide a generalized constitutive model accounting for the static and flowing behaviors of granular materials under either steady or transient conditions [1].

Despite the fruitful discussions on dry granular collapses, the knowledge of immersed granular collapses remains limited. One major source of difficulty is the complicated interplay among a number of factors that control the collapse dynamics. Such factors include the initial aspect ratio [26–28], the initial packing density [26,29–34], particle size [28,35–37], particle density [38], and fluid viscosity [27,28]. Different combinations of these factors can lead to a large variety of flow regimes, where either viscous dissipation, fluid inertia, or grain inertia may dominate [27,28,35,39]. Here, we focus on a single controlling parameter, i.e., the initial aspect ratio, the role of which still remains unclear in the immersed situation [26,27]. We restrict the choice of ambient fluid to water, and compare all underwater cases with their dry counterparts. This specific choice simplifies the flow regimes to be encountered (i.e., the fluid-inertial regime [27]), thus allowing us to concentrate on the role of aspect ratio. In fact, even this single type of fluid leads to distinct dynamics during the collapse of shallow and tall columns. To give a full picture of the problem under consideration, we present and discuss results on flow dynamics, scaling arguments, deposit morphology, and the evolution of energy. Particularly, we associate the transition of scaling laws with the energy

*fiona.kwok@hku.hk

conversion in vertical and horizontal directions. The internal flow properties (e.g., particle velocity, fluid velocity, and energy conversion) are made accessible by employing a coupled continuum-discrete method. The details of our numerical model are given in Sec. II. Then, typical collapse dynamics are presented in Sec. III, followed by the quantitative results regarding scaling arguments (Sec. IV) and energy analyses (Sec. V). Conclusions are drawn in Sec. VI.

II. NUMERICAL METHODOLOGY

A. Numerical model and validation

We use a coupled continuum-discrete method that combines coarse-grid computational fluid dynamics (CFD) and discrete element method (DEM). The CFD-DEM model has the advantage of solving fluid-particle interactions at a low computational cost, allowing efficient three-dimensional simulations [40,41]. Details of the CFD-DEM method are given in Appendix.

Our CFD-DEM coupling is implemented with a combination of open source C++ libraries, namely, OPENFOAM [42] and CFDEMPROJECT [41]. We have performed detailed validations for this CFD-DEM framework against multiple benchmark problems in our previous work [43]. Recently, the CFDEMPROJECT software has been widely applied in the study of immersed granular flows, such as the sandpile formation in water [44], the formation of landslide dams in rivers [45], and immersed hopper flows [46]. In this study, since we do not aim to reproduce the exact details of any laboratory experiments, we choose the model setup and parameters based on general choices in the literature (specified in the next subsection). As we shall see later in Sec. IV C, our numerical results have good agreement with published experimental data and theoretical arguments.

B. Model setup and parameters

The setup of our numerical experiments is illustrated in Fig. 1(a). The computational domain is a rectangular box of length L, width W, and height H, filled with fluid. Periodic boundaries are imposed on the two sides of the domain in both CFD and DEM, resulting in a quasi-two-dimensional configuration. In DEM, the bottom of the box is roughened by gluing a layer of base particles (diameter d_b). A granular column (particle diameter d_p) is generated with an initial length l_i and height h_i, hence an initial aspect ratio $a = h_i/l_i$ [Fig. 1(b)]. The coordinate system of this quasi-two-dimensional problem is shown in Fig. 1(c), with the front position x_f and top height y_t given for time t after the release of the initial mass. Eventually, the granular mass comes to a final stop as shown in Fig. 1(d), where the final length l_f and height h_f can be obtained. Note that the runout distance is conventionally defined as $l_f - l_i$, and h_f is measured at $x = 0$. The final thickness in the middle region, h_f^m, is also measured at $x = 0.5l_f$ for later analyses.

The specific choices of parameters are elaborated as follows. We use particle diameter $d_p = 0.001$ m, with a slight polydispersity (Gaussian distribution with standard deviation of $0.1d_p$) to avoid layering, initial length $l_i = 20d_p$, and aspect ratio $a \in [0.5, 8]$. The bulk packing density of the initial columns is around 0.56. The length and height of the computational domain (L and H) are adjusted for each a to avoid boundary effects; for instance, we have $L = 20l_i$ and $H = 10l_i$ for $a = 8$. The separation of periodic boundaries remains unchanged ($W = 10d_p$), which has been verified to be sufficient to not affect the results. The rough bottom is made of closely packed base particles with $d_b = d_p$, which is comparable to the roughness size used in previous experiments [8,9]. Since the influence of base roughness was reported to be minor [8,9], we do not vary d_b in this study. However, we note that our recent work [47] suggested a stronger basal effect in steady flows if a much wider range of roughness is adopted (by varying d_b and spacing), which is worth a future investigation with the current transient configuration.

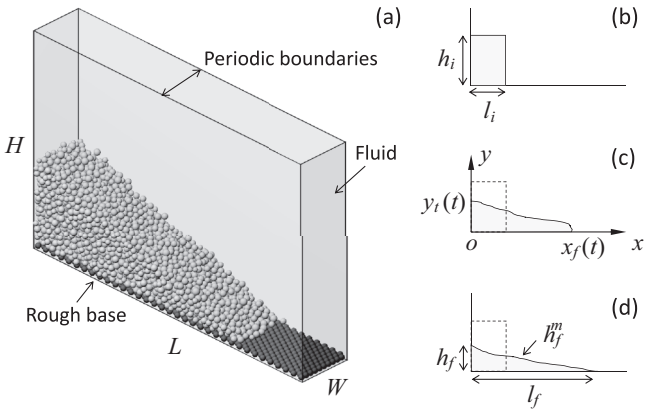

FIG. 1. Setup and primary notation. (a) The three-dimensional model in CFD-DEM, with a computational domain of size $L \times W \times H$. Periodic boundaries are imposed in the width direction. The bottom is roughened by a layer of fixed particles. (b) Initial configuration with initial length l_i and height h_i. (c) Front position $x_f(t)$ and top height $y_t(t)$ at an arbitrary time t. (d) Final configuration with final length l_f and height h_f (measured at $x = 0$). The middle deposit thickness h_f^m is measured at $x = 0.5l_f$.

For each aspect ratio, we run two parallel simulations under dry (DEM only) and underwater (CFD-DEM) conditions, respectively. In DEM, the particle properties are consistent for both bulk and base particles: particle density $\rho_p = 2650$ kg/m^3, Young's modulus $Y = 5$ GPa, Poisson's ratio $\nu = 0.24$, the coefficient of friction $\mu_p = 0.5$, and the coefficient of restitution $e = 0.5$. The Young's modulus is one order of magnitude smaller than that of actual glass beads (i.e., 50 GPa), which does not affect the results but significantly saves computational time [15]. Although the choice of e is smaller than the measured value (around 0.8) of glass beads [48], we have verified that varying e leads to nearly identical final deposits for both dry and underwater cases, but a moderate value (i.e., $e = 0.5$) has the advantage of reducing computational efforts and producing more realistic interactions between frontal particles and the bumpy bottom. The friction parameter $\mu_p = 0.5$ follows general choices. In fact, a previous study showed that only extreme values of the contact parameters ($e \to 1$ or $\mu_p \leqslant 0.1$) induce substantial influence on the overall collapse behaviors [14]. In CFD, the fluid is set as pure water with density $\rho_f = 1000$ kg/m^3 and

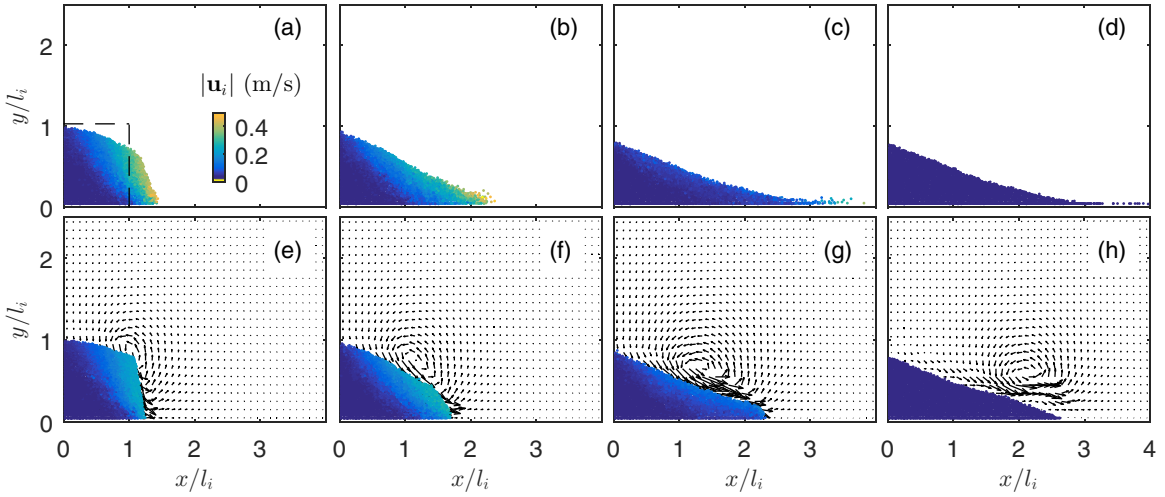

FIG. 2. Snapshots of granular collapse with $a = 1$. From left to right: $t = 0.05, 0.10, 0.20, 0.50$ s. (a)–(d) Dry. (e)–(h) Underwater. The color map indicates the magnitude of velocity of individual particles ($|\mathbf{u}_i|$), while the arrows in the lower panels represent the fluid velocity field of a central slice. The fixed layer of base particles are not shown.

viscosity $\mu_f = 0.001$ Pa s. The size of computational cells in CFD is $2d_p$, and we have verified the numerical convergence towards this resolution. The time steps in DEM and CFD are 10^{-6} s and 10^{-5} s, respectively, such that coupling is made every 10 DEM cycles [41,43].

III. COLLAPSE DYNAMICS OF SHALLOW AND TALL COLUMNS

We present two distinct collapse behaviors of shallow ($a = 1$) and tall ($a = 8$) columns in Secs. III A and III B, respectively. Each underwater case is compared with its dry counterpart.

A. Collapse of shallow columns

Figure 2 presents the collapse of shallow columns ($a = 1$) under dry and underwater conditions. The initial state of both cases is shown as a dashed profile in Fig. 2(a).

In the dry case, flow starts from the leading edge [Fig. 2(a)], with a clear boundary (or, a fracture surface) indicated by the velocity distribution between mobilized and stationary zones. The flow is localized above the fracture surface. As the granular flow propagates, its front becomes thinner, forming a sharp tip, and the flowing layer becomes shallower towards the surface [Figs. 2(b) and 2(c)]. Since the front particles have less contact with their neighbors, a small number of them may become detached from the main flow [Fig. 2(c)]. Eventually, the flow comes to a halt and the final deposit exhibits a triangular shape with a slightly concave surface [Fig. 2(d)].

Compared to the dry case, the underwater collapse has a similar fracturing process with a longer duration and shorter runout distance. Several unique characteristics can be observed. The particle flow initiated at the top-right corner leads to the formation of a vortex in the ambient fluid [Fig. 2(e)], which propagates in the direction of the overall motion of particles. A thicker front of the granular flow is built up followed by a convex surface, which is attributed to the resistance (i.e., drag force) provided by the fluid [Fig. 2(f)]. The convex front contrasts with the sharp tip in the dry collapse, and sustains during the deposition stage [Figs. 2(g) and 2(h)]. The convexity clearly modifies the surface shape of the final deposit, as seen by comparing Figs. 2(d) and 2(h). The resistance of fluid also leads to a denser front where no detached particles can be observed. In the final state where all particles reach an equilibrium, the vortex continues to flow away from the granular deposit [Fig. 2(h)].

B. Collapse of tall columns

Figure 3 presents the collapse of tall columns ($a = 8$) under dry and underwater conditions. The initial profile (dashed line) is shown in Fig. 3(a).

The collapse of tall columns is more complicated than the shallow ones. Three clear stages emerge subsequently, namely, collapse, heap, and spread [27]. A distinct vertical fall can be observed in the initial stage [Figs. 3(a) and 3(e)]. The motion of particles near the top surface is similar to a free fall [10], which will be discussed quantitatively in Sec. IV B. Horizontal displacement is not significant in this stage [19]. For this reason, the recirculation of fluid (i.e., vortex formation) at the top corner is not significant during the fall of particles.

The particles then heap up and turn into a shear flow. The majority of the column mass has been involved during the heaping, with only a relatively small "dead zone" observed at the bottom-left corner in both cases [Figs. 3(b) and 3(f)]. The granular heap then starts to spread horizontally. In the dry case, the frontal region is followed by a significant concave flow-depth profile [such as $x/l_i = 4$ in Fig. 3(c)]. In contrast, a much thicker front can be observed in the underwater case, and some "clouds" of particles are observed on the surface with the water flow [Fig. 3(g)]. A major eddy starts to develop in the fluid, as the granular flow evolves from falling to spreading. The front position under the underwater condition is significantly behind that of the dry collapse [Figs. 3(c) and 3(g)].

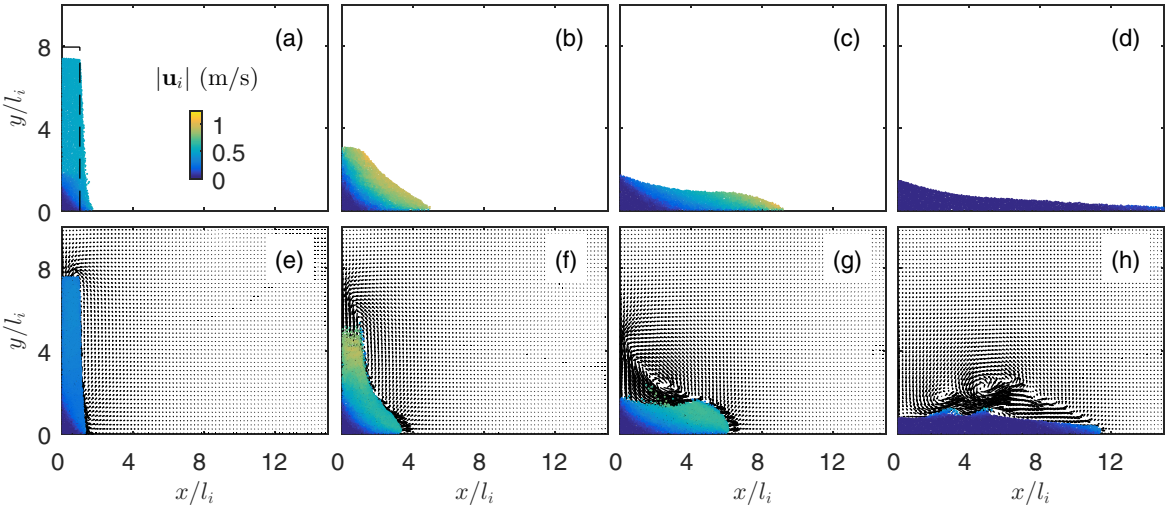

FIG. 3. Snapshots of granular collapse with $a = 8$. From left to right: $t = 0.05, 0.15, 0.25, 0.50$ s. (a)–(d) Dry. (e)–(h) Underwater. The color map indicates the magnitude of velocity of individual particles ($|\mathbf{u}_i|$), while the arrows in the lower panels represent the fluid velocity field of a central slice. The fixed layer of base particles is not shown.

In the final configuration, the dry deposit shape is roughly triangular with a long sharp tip and concave surface [Fig. 3(d)], while the underwater deposit exhibits a complicated morphology [Fig. 3(g)]. A nonmonotonic surface [see, e.g., $x/l_i = 3 - 5$ in Fig. 3(h)] is formed as the loosely packed particles on the surface are eroded and further transported by the fluid flow. A typical moment of this phenomenon is presented in Fig. 4.

IV. SCALING ARGUMENTS AND FINAL DEPOSITS

In the following, we explore more quantitative data over a wide range of aspect ratios. We present the temporal evolution of the front position and column height in Secs. IV A and IV B, respectively, and then focus on the scaling laws in Sec. IV C. In Sec. IV D, we discuss the effects of fluid on the deposit morphology.

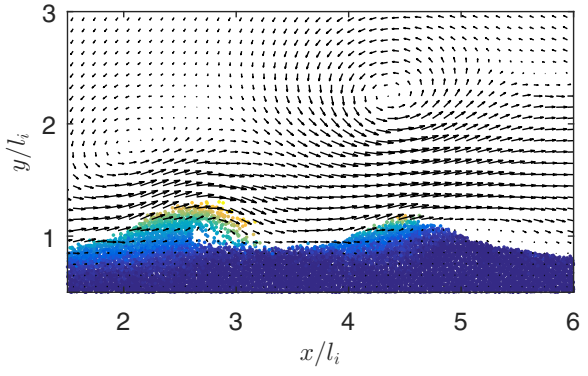

FIG. 4. Transport of particles on the deposit surface by the fluid. The arrows indicate the velocity vectors of the fluid, while the points with dark to bright colors represent particles with low (zero) to high velocities.

A. Front propagation

Figure 5 compares the front propagation in dry (left panels) and underwater (right panels) cases for varying aspect ratios $a = 0.5, 1, 2, 4, 8$. In Figs. 5(a) and 5(b), physical units are used for both front position x_f and time t. Comparing the stoppage time for different a, which is marked by a circle on each line, it is apparent that the flow duration increases with a, and that the front propagation is slightly slowed down in the underwater cases. Note that the stoppage time is determined with x_f only (when the change of x_f is no longer greater than $0.01d_p$), which does not account for the remaining motion of particles behind the front. The kinks in the deposit stage for dry cases [such as $t \approx 0.45$ s, $a = 8$ in Fig. 5(a)] are due to the detachment of particles in the frontal regions (detached particles are excluded when x_f is determined). By contrast, the lines for underwater cases are smoother because all particles remain in the bulk, especially for taller columns [Fig. 5(b)].

Outstanding features of the front propagation is the three stages of acceleration, constant velocity, and deceleration [8,10,36]. From Figs. 5(a) and 5(b), we observe a similar initial acceleration stage for all aspect ratios in both dry and underwater cases. The constant acceleration is previously reported as $0.75g$ in dry experimental collapses [10], which matches well with the value in our dry cases [Fig. 5(a)]. Interestingly, by using a reduced gravity $g' = (\rho_p - \rho_f)g/\rho_p$, which accounts for the buoyancy effect in the ambient fluid, the underwater accelerations are also a constant, $0.75g'$, as shown in Fig. 5(b). The converged initial behavior of shallow and tall columns seems to stem from the fact that the *initial* propagation of the lower part of a tall column does not interact with the vertical motion of its upper part. Indeed, in the initial stage, the energy dissipation due to particle interactions is negligible (see Sec. V C). Moreover, the constant values of $0.75g$ and $0.75g'$, which are surprisingly coincident, may be explained by a similar basal resistance provided by the same rough bottom. After the initial acceleration in

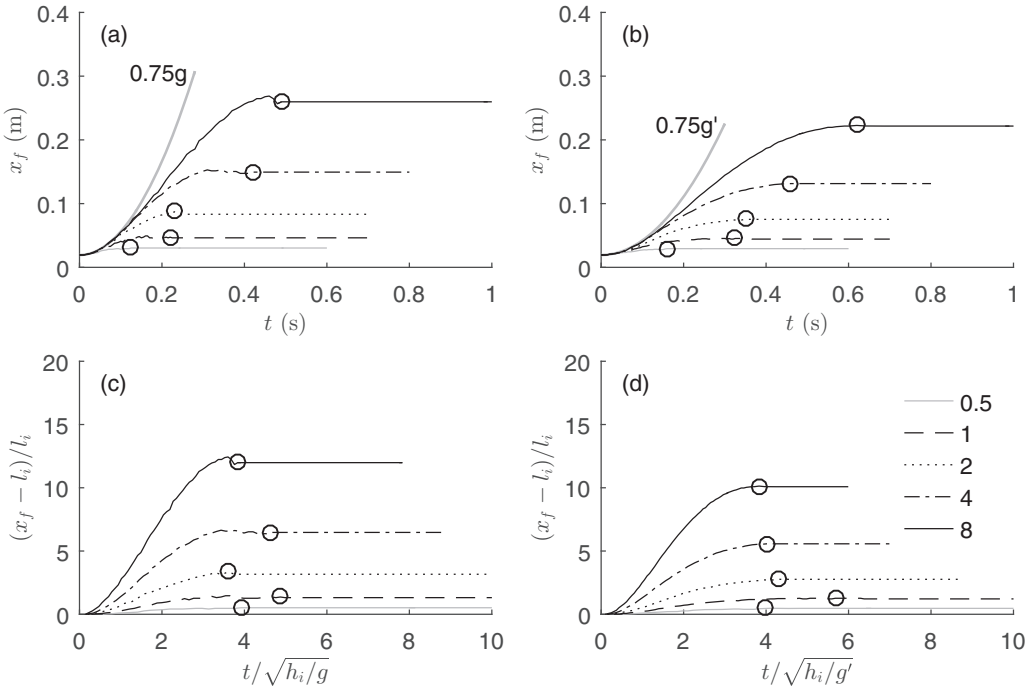

FIG. 5. Front propagation of dry (left panels) and underwater (right panels) cases, with varying aspect ratios ($a = 0.5, 1, 2, 4, 8$). Circular markers indicate the stoppage time when the change of x_f is smaller than $0.01d_p$. (a), (b) The front position x_f as a function of time t with physical units. The gray thick lines show the acceleration of $0.75g$ and $0.75g'$, respectively. (c), (d) The normalized front position $(x_f - l_i)/l_i$ against the normalized time $t/\sqrt{h_i/g}$ and $t/\sqrt{h_i/g'}$ for dry and underwater cases, respectively.

Figs. 5(a) and 5(b), the front propagates at a relatively constant velocity for each a, until it decelerates and stops. The duration of the constant-velocity stage increases with a, agreeing with previous results [10,12].

Next, we explore the front propagation in terms of dimensionless variables. Previous work showed that by choosing a timescale $\sqrt{h_i/g}$, the total durations of dry granular collapses become a constant, regardless of the aspect ratio [8,10]. For immersed granular collapses, the timescale $\sqrt{h_i/g'}$ was shown to be proper [36]. As for the length scale, a common choice in the literature is to normalize the travel distance $x_f - l_i$ by l_i [8,12]. Here, we follow this length scale, but also discuss an alternative scaling later. The scaled results are shown in Figs. 5(c) and 5(d). In agreement with the literature, we observe that after normalization the total flow durations become close for both dry and underwater cases. The dimensionless duration was previously reported as 3.3 in [8,10], while in our cases it lies around 4. On the other hand, the normalized form of front position $(x_f - l_i)/l_i$ preserves the influence of aspect ratio; a higher a leads to a longer $(x_f - l_i)/l_i$ [8].

Alternatively, we rescale the travel distance by the initial column height, i.e., $(x_f - l_i)/h_i$, since the collapse is essentially driven by the initial potential energy of a column. The use of h_i as length scale is also compatible with the timescale $\sqrt{h_i/g}$ or $\sqrt{h_i/g'}$. As seen in Figs. 6(a) and 6(b), an outstanding similarity of collapse behaviors is achieved for a wide range of a, except the very shallow column $a = 0.5$ which has a very short constant acceleration in the beginning. The constant initial acceleration of 0.75 is recovered in its dimensionless form in both dry and underwater cases. Further, we use a velocity scale $\sqrt{gh}$ or $\sqrt{g'h}$ to normalize the frontal velocity u_f, as presented in Figs. 6(c) and 6(d). The dimensionless front velocities are nearly identical (except $a = 0.5$), showing clearly the acceleration, constant-velocity, and deceleration stages. The rescaled results in Fig. 6 suggest a large dynamic similarity in the front propagation of different columns, even with different ambient environments. Noting that the overall collapse dynamics is distinct for different aspect ratios (see Sec. III), the similarity of front propagation shows that the frontal region communicates marginally with the flow behind it and, therefore, in order to clearly characterize the flow dynamics, other measurements and flow properties should be studied. Next, we discuss flow thickness and deposit morphology, following which is a detailed analysis on energy evolution (Sec. V).

B. Evolution of column height

Another quantity characterizing the dynamic deformation of collapsing columns is the top height y_t at $x = 0$, which is defined in Fig. 1(c). Figures 7(a) and 7(b) present y_t as a function of t for $a = 1, 2, 4, 8$ under dry and underwater conditions, respectively. For smaller a, the variation of y_t is subtle and gradual, while for larger a, a dramatic decrease in y_t is observed, known to be ballistic (free fall) in the literature [10,11]. The initial free-fall behavior for large a can be shown clearly with the dimensionless variables. In Figs. 7(c) and 7(d), the normalized top height y_t/h_i is plotted against $t/\sqrt{h_i/g}$ and $t/\sqrt{h_i/g'}$ for dry and underwater cases, respectively. The initial falls for $a = 4$ and 8 match perfectly with the free-fall trajectory with a dimensionless acceleration

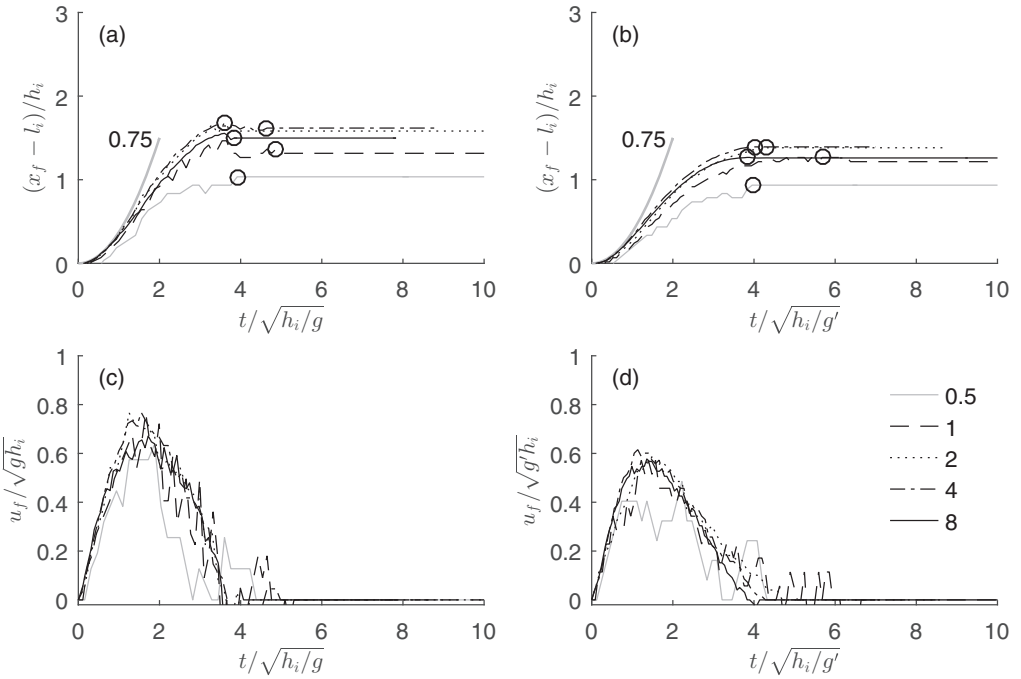

FIG. 6. Normalized front position and frontal velocity as a function of time for dry (left panels) and underwater (right panels) cases, with varying aspect ratios ($a = 0.5, 1, 2, 4, 8$). (a), (b) Normalized front position $(x_f - l_i)/h_i$ against normalized time $t/\sqrt{h_i/g}$ and $t/\sqrt{h_i/g'}$, respectively. The gray thick lines show the acceleration of 0.75 in its dimensionless form. Circular markers indicate the stoppage time when the change of x_f is smaller than $0.01d_p$. (c), (d) Normalized frontal velocity $u_f/\sqrt{gh_i}$ and $u_f/\sqrt{g'h_i}$ for dry and underwater cases, respectively.

of 1. The only exception is the $a = 8$ case in water, where the fall deviates slightly after a short period of time. A closer look at Figs. 3(e) and 3(f) suggests that the shape of the top surface deforms due to the interaction with fluid, which indicates the influence of emerging drag forces along with the development of particle-fluid relative velocity.

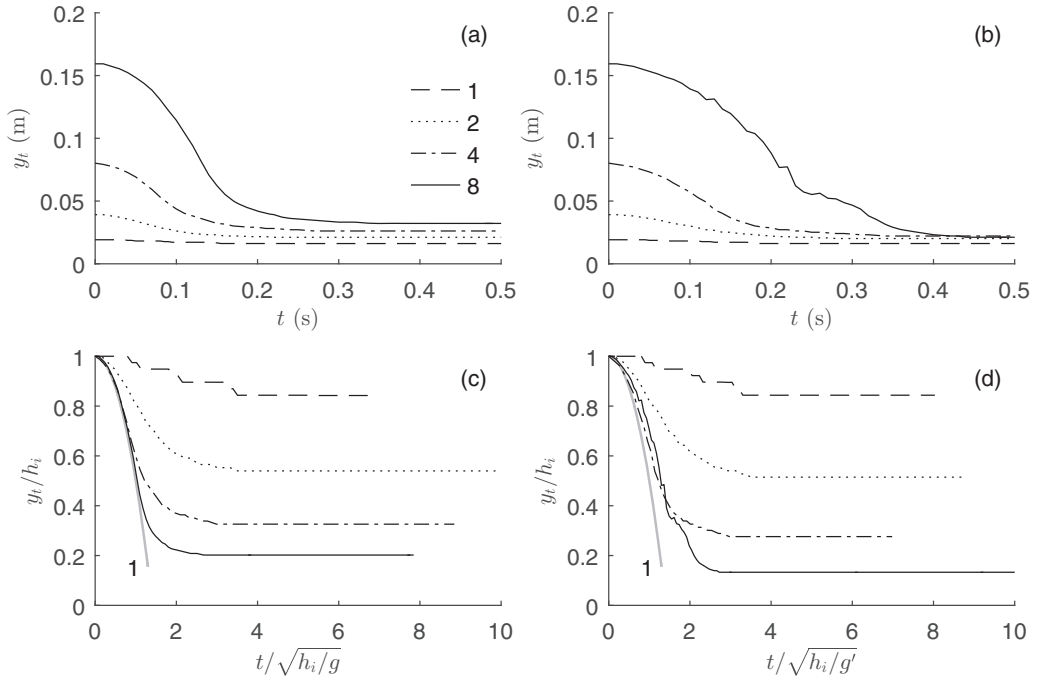

FIG. 7. Evolution of the height of top surface (y_t) measured at $x = 0$, for dry (left panels) and underwater (right panels) cases with varying aspect ratios ($a = 1, 2, 4, 8$). (a), (b) y_t as a function of t with physical units. (c), (d) The normalized top height y_t/h_i against the normalized time $t/\sqrt{h_i/g}$ and $t/\sqrt{h_i/g'}$ for dry and underwater cases, respectively. The gray thick lines imply the free-fall acceleration of 1 in its dimensionless form.

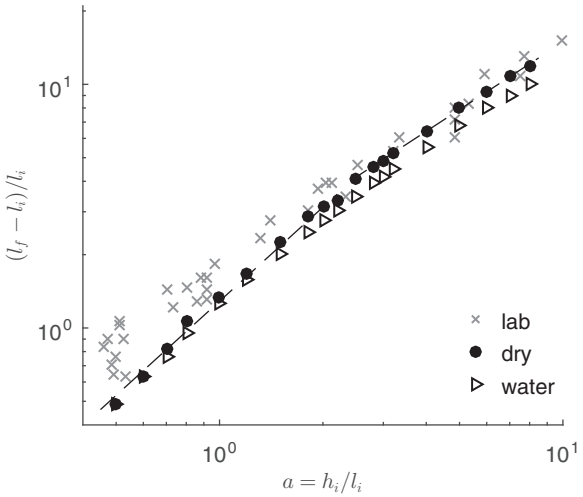

FIG. 8. Normalized runout distance $(l_f - l_i)/l_i$ as a function of the initial aspect ratio $a = h_i/l_i$. The laboratory data (indicated by "lab") are the results of dry granular collapse from the work of Lajeunesse *et al.* [8]. The dashed lines are power-law fittings for dry cases [see Eq. (1)]. Error bars obtained from five repeated simulations with varying random seeds are smaller than the symbol size (hence not shown) for cases $a = 0.5, 0.6, 0.8, 1, 6$ under both dry and underwater conditions.

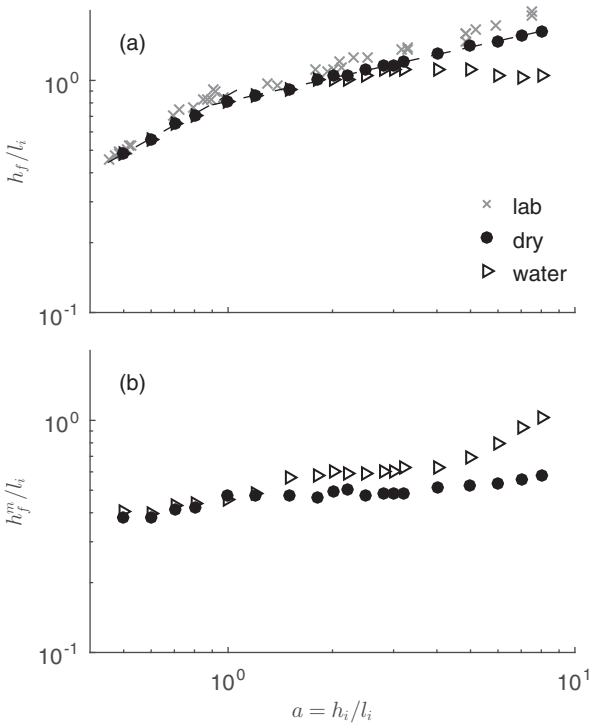

FIG. 9. Final thickness as a function of the initial aspect ratio $a = h_i/l_i$. (a) Normalized deposit thickness h_f/l_i measured at $x = 0$. The dashed lines are power-law fittings for dry cases [see Eq. (2)]. The laboratory data (indicated by "lab") are the results of dry granular collapse from the work of Lajeunesse *et al.* [8]. (b) Normalized *middle* deposit thickness h_f^m/l_i, which is measured at $x = 0.5l_f$. Error bars obtained from five repeated simulations with varying random seeds are smaller than the symbol size (hence not shown) for cases $a = 0.5, 0.6, 0.8, 1, 6$ under both dry and underwater conditions.

C. Scaling laws with aspect ratio

In this section, we focus on the final runout distance (l_f) and deposit thickness (h_f). In Fig. 8, $(l_f - l_i)/l_i$ is plotted as a function of a. For the dry cases, a piecewise power-law relation is observed with the change of slope occurring at around $a = 2.5$, in agreement with previous experimental and numerical results [8,10,12]. This may be explained by the change of flow behavior when vertical inertia becomes significant for taller columns (see Sec. III). For the underwater cases, the scaling relation between $(l_f - l_i)/l_i$ and a slightly tilts downwards since the ambient fluid tends to provide resistance to particles through drag forces. A smoother change of slope is observed at $a = 2 \sim 3$.

Although we do not aim to reproduce the details of any existing experiments, the general power-law relations match with the experimental data from Lajeunesse *et al.* [8]. Our results show a shorter runout when a is small, but a slightly quicker growth as a increases; the agreement at large values of a is excellent (Fig. 8). Our data for dry cases can be fitted with the following power-law curves

$$\frac{l_f - l_i}{l_i} = \begin{cases} 1.29a^{1.28}, & a \in [0.5, 2.5) \\ 1.8a^{0.92}, & a \in [2.5, 8] \end{cases} \quad (1)$$

in which the exponents for shallow ($a < 2.5$) and tall columns ($a \geqslant 2.5$) are 1.28 and 0.92, respectively, slightly larger than those (1 and $\frac{2}{3}$, respectively) reported in [8] and other experimental studies (a recent summary of the scaling laws can be found in [1]). The discrepancy between our simulations and the laboratory data may stem from several sources. On one hand, the treatment of rough bases differs in laboratory tests and numerical simulations. In [8], the base was lined with a piece of sandpaper, while we use a layer of fixed particles. The roughness size is larger in our simulations, which may explain the shorter runout distance for shallow columns. A detailed calibration on particle parameters may be necessary to reproduce the roughness in the simulations, due to the difference of material properties, which is however not the focus of this study. On the other hand, the quicker growth (i.e., larger exponents) may be attributed to the fact that we use perfectly spherical particles, without the use of rolling resistance to account for shape effects [15], which allows a higher mobility compared to the glass beads in the laboratory. Moreover, the experimental observations in [8] were made from the side wall, which slightly restrained the motion of particles by providing additional friction. In contrast, we use periodic boundaries at the two sides, leading to a quasi-two-dimensional situation with no such sidewall effects. Interestingly, the exponent of 0.92 for tall columns in our fitting matches well with the value of 0.9 ± 0.1 obtained with a wide channel, where sidewall effect shall be minimized [11].

Figure 9(a) presents the deposit thickness h_f/l_i as a function of a. Note that as a convention for dry granular collapses in the literature, h_f/l_i is measured at $x = 0$ and is known as the maximum thickness (which may not be true for very tall columns with $a > 10$; see [4]). In underwater cases, our results show that h_f at $x = 0$ is usually not the maximum thickness due to the more complicated deposit morphology

resulting from fluid-particle interactions. Nevertheless, we first compare our data of h_f/l_i with the laboratory measurements [8]. For dry cases, we have

$$\frac{h_f}{l_i} = \begin{cases} 0.87a^{0.84}, & a \in [0.5, 1) \\ 0.81a^{0.33}, & a \in [1, 8] \end{cases} \tag{2}$$

in which the exponent 0.33 for $a \geqslant 1$ matches well with the experimental value ($\frac{1}{3}$ for $a \geqslant 0.7$) in [8]; for $a < 1$, the fitted exponent in our cases is 0.84, smaller than the experimental value of 1. Similar scaling laws from previous studies have been summarized in [1]. In general, the thickness is slightly higher in the experiments, which is again attributed to the side-wall effect that the wall friction tends to restrain the fall of particles and the shape effect of spherical particles.

For underwater cases, the difference caused by water is negligible when $a < 2$, while a significant change occurs as a reaches 4 [Fig. 9(a)]. As explained earlier, during the collapse of tall columns, the propagation of eddies in the flow direction transports particles from the vicinity of $x = 0$ to further locations, resulting in the substantial decrease of h_f/l_i at $x = 0$. Since the transported particles tend to settle around the middle region of the deposit [see Fig. 3(h)], we compare additionally the final deposit thickness at $x = 0.5l_f$, which is denoted by h_f^m. As seen in Fig. 9(b), h_f^m is generally higher in underwater cases, which becomes obvious when $a > 1$ and increases significantly when $a \geqslant 4$.

D. Deposit morphology

In the existing studies on dry granular collapses, l_f and h_f are sufficient to represent the deposit morphology [8,10,11]. However, the presence of an ambient fluid may substantially modify the shape of a deposit surface, owing to the complicated fluid-particle interactions, such as eddy formation and surface erosion. Here, we illustrate the modified surface morphology with a direct comparison between dry and underwater cases (Fig. 10). When $a = 1$ and 2, the deposit shapes are nearly identical in dry and underwater cases. When $a = 4$, 6, 8, the thickness at $x = 0$ declines, and more material is deposited in the middle areas. For tall columns, the footprint of surface erosion by fluid eddies (Fig. 4) can be found in the morphology of their deposit surface (Fig. 10).

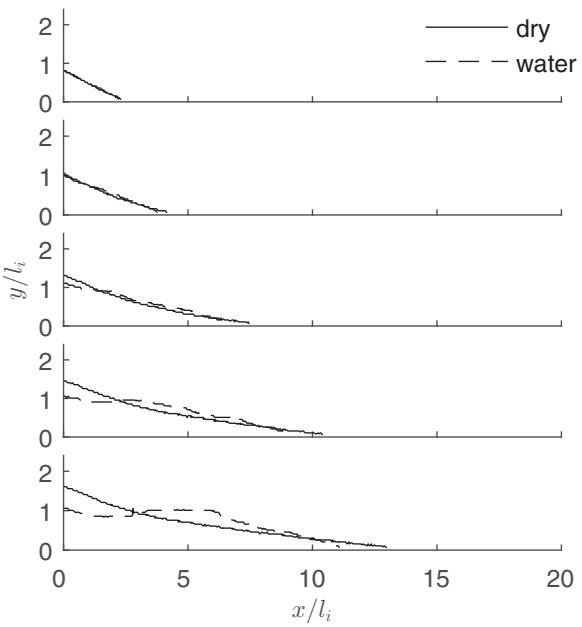

FIG. 10. Comparison of deposit morphology between dry and underwater cases. From top to bottom: $a = 1, 2, 4, 6, 8$, respectively.

V. ENERGY CONVERSION AND DISSIPATION

As addressed earlier, the data of runout distance and deposit thickness can hardly provide a full picture of the complicated collapse dynamics especially when an ambient fluid is involved. In this section, we define different forms of energy (Sec. V A) and then detail their evolution for shallow (Sec. V B) and tall (Sec. V C) columns. Furthermore, we discuss the energy transformation from potential to kinetic forms during the collapse of columns (Sec. V D) and the energy conversion from vertical to horizontal directions (Sec. V E).

A. Different forms of energy

The temporal evolution of kinetic energy has been used to understand the dynamics of dry granular collapses [2,12,13,16,27]. As a collapse occurs, the dynamics of the whole system is driven by the drop of potential energy of particles (assuming a negligible change of potential energy in the fluid). The total potential energy E_p is defined as

$$E_p = \sum_{i=1}^{n_p} m_i g h_{ci}, \tag{3}$$

where m_i and h_{ci} are the mass and centroid height of a particle i, respectively, and n_p is the total number of particles. Since E_p is a function of time, i.e., $E_p = E_p(t)$, we can define the total initial potential energy as $E_0 = E_p(0)$. The *cumulative* energy converted from potential energy at time t is then

$$\Delta E_p = E_0 - E_p(t). \tag{4}$$

During a collapse, the change of potential energy, ΔE_p, is either transformed into the kinetic energy of particles and fluid, or it is dissipated due to inelastic particle interactions (i.e., sliding and damping) and fluid viscosity. Here, we ignore the elastic potential energy stored at contacts and do not calculate the nontrivial details of energy dissipation. Instead, we explore the energy dissipation by comparing ΔE_p with the total kinetic energy gained in particles and fluid, i.e., E_k^p and E_k^f, such that the *cumulative* dissipated energy is approximately

$$E_d = \Delta E_p - E_k^p - E_k^f \tag{5}$$

with E_k^p and E_k^f given by

$$E_k^p = \frac{1}{2}\sum_{i=1}^{n_p} m_i |\mathbf{u}_i|^2, \tag{6a}$$

$$E_k^f = \frac{1}{2} V_{fc} \sum_{i=1}^{n_{fc}} \rho_f |\mathbf{u}_f|^2, \tag{6b}$$

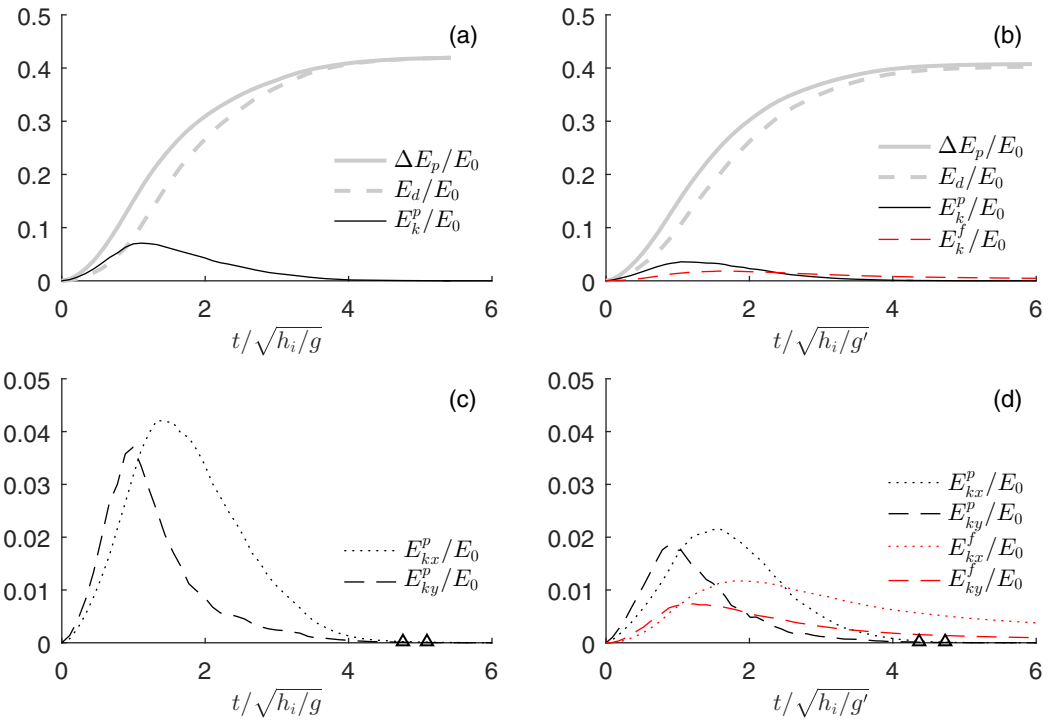

FIG. 11. Evolution of normalized energy for $a = 1$ under dry (left panels) and underwater (right panels) conditions. (a), (b) Total kinetic energy of particles (and fluid, if applicable), compared with the energy converted from total potential energy. (c), (d) Partial kinetic energy of particles (and fluid, if applicable) computed from the velocity components in x and y directions. The triangular markers indicate the time when kinetic energy becomes negligible (i.e., smaller than $10^{-4}E_0$).

where $|\mathbf{u}_i|$ is the magnitude of the velocity of particle i (of which there are n_p), $|\mathbf{u}_f|$ is the magnitude of local fluid velocity, and V_{fc} is the volume of a fluid cell (of which there are n_{fc}). Note that the rotational kinetic energy is ignored in this analysis, which has been found to be minor during granular collapses [2]. Indeed, we have verified that the rotational kinetic energy is typically smaller than $10^{-3}E_0$ in all present cases.

Next, to distinguish the different stages where a redirection of the main flow takes place, "partial" kinetic energies are calculated by considering horizontal and vertical velocity components [12,16,27]. For particles, we have

$$E_{kx}^p = \frac{1}{2}\sum_{i=1}^{n_p} m_i u_i^2, \tag{7a}$$

$$E_{ky}^p = \frac{1}{2}\sum_{i=1}^{n_p} m_i v_i^2, \tag{7b}$$

where u_i and v_i are velocities of particle i in x and y directions, respectively. For fluid, we have

$$E_{kx}^f = \frac{1}{2}V_{fc}\sum_{i=1}^{n_{fc}} \rho_f u_f^2, \tag{8a}$$

$$E_{ky}^f = \frac{1}{2}V_{fc}\sum_{i=1}^{n_{fc}} \rho_f v_f^2, \tag{8b}$$

where u_f and v_f are local fluid velocities in x and y directions, respectively. Note that the partial kinetic energy based on transversal velocities (in z direction) is negligible for both particles and fluid (typically smaller than $10^{-3}E_0$).

B. Energy evolution of shallow columns

Figure 11 presents the energy evolution for $a = 1$ columns under dry (left panels) and underwater (right panels) conditions. All energy forms are normalized by the energy scale E_0, such that their values represent a fraction of the total initial potential energy.

The first row of Fig. 11 presents the conversion from potential energy to kinetic energy in particles and fluid. In both dry and underwater cases, only about 40% of the initial potential energy is involved in the dynamic process since the center of mass of the shallow columns falls a relatively small distance (see Fig. 2). The kinetic energy, which represents a small portion of the initial potential energy (less than 10%), increases to a peak at around 1 characteristic time, and then fades away at around 4. By comparing dry [Fig. 11(a)] and underwater cases [Fig. 11(b)], the overall energy dissipation (E_d) evolves similarly. Between the fluid and particles [Fig. 11(b)], energy transfer takes place from particles to water through interactions, resulting in a lower particle kinetic energy (E_k^p) along with the increase of fluid kinetic energy (E_k^f).

The second row of Fig. 11 shows the partial kinetic energy in x and y directions. In both dry and underwater cases, the vertical and horizontal movements develop roughly

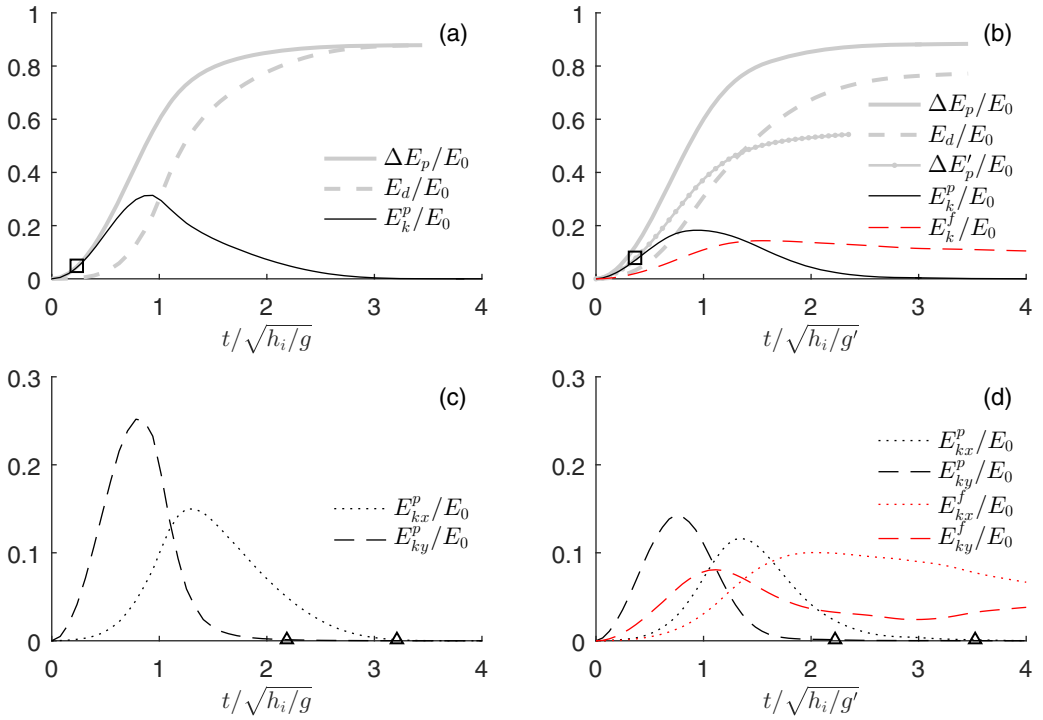

FIG. 12. Evolution of normalized energy for $a = 8$ under dry (left panels) and underwater (right panels) conditions. (a), (b) Total kinetic energy of particles (and fluid, if applicable), compared with the energy converted from total potential energy. The square markers indicate the time when granular dissipation starts. (c), (d) Partial kinetic energy of particles (and fluid, if applicable) computed from the velocity components in x and y directions. The triangular markers indicate the time when kinetic energy becomes negligible (i.e., smaller than $10^{-4}E_0$).

simultaneously, which correspond to the fracturing behavior in Fig. 2, where particles slide down a self-formed slope that is associated with their frictional property [11]. By closely comparing E_{kx}^p (or E_{kx}^f) and E_{ky}^p (or E_{ky}^f), the partial kinetic energy in the vertical direction evolves faster and reaches its peak slightly earlier, while the peak in the horizontal direction is higher. The vertical energy evolution becomes insignificant (but not zero) after around 2 characteristic times, in contrast to the horizontal evolution that remains active for a longer duration. The time when E_{kx}^p and E_{ky}^p completely vanish is roughly the same [see the triangular markers in Figs. 11(c) and 11(d)]. The observations indicate that for the small aspect ratio $a = 1$, the horizontal spreading is more significant than the vertical falling, albeit both processes are present until the end of the flow.

C. Energy evolution of tall columns

Figure 12 presents the energy evolution for $a = 8$ columns under dry (left panels) and underwater (right panels) conditions. The first row compares the change of total potential energy (ΔE_p), total energy dissipation (E_d), and the total kinetic energy of particles (E_k^p) and fluid (E_k^f), from which we observe several distinct features related to the high aspect ratio. First, around 90% initial potential energy is utilized during the collapse of tall columns. As seen in Fig. 3, nearly all particles have been mobilized within the initial fall stage, and the relative height drop of the overall center of mass is substantially larger than that of previous shallow columns. Second, more kinetic energy is gained in the system when compared to the shallow columns. The overall energy dissipation E_d is much lower in Fig. 12(b) than in Fig. 12(a), and the motion of fluid continues for a long time after the granular pile comes to a equilibrium; see the vortex propagation in Fig. 3(h). In other words, a considerable portion of energy has been transferred to the fluid, which is then dissipated gradually by viscosity.

Another outstanding feature of the collapse of tall columns is the delay of energy dissipation, as seen in Fig. 12(a). In the initial stage where particles mainly fall freely under gravity [Fig. 7(c)], E_d remains close to zero (and E_k^p overlaps with ΔE_p) for around 0.2 characteristic time [see the square marker in Fig. 12(a)]. It indicates that in this stage particles fall in block, and the initial potential energy is mainly converted to the kinetic energy of particles; particle interactions only dissipate a negligible amount of energy. Energy dissipation starts when falling particles impact the bottom, companioned by a more substantial horizontal spreading [see such a moment in Fig. 3(b)].

In the underwater case [Fig. 12(b)], such a dissipation-free stage is not seen by simply comparing ΔE_p and E_k^p. Energy is dissipated since the start. However, it is not clear whether this dissipation is due to particle interactions or fluid viscosity. To understand this, we define a *reduced* potential energy E_p' and its cumulative change $\Delta E_p'$, which are

$$E_p' = \sum_{i=1}^{n_p} m_i g' h_{ci}, \tag{9a}$$

$$\Delta E_p' = E_p'(0) - E_p'(t), \tag{9b}$$

where $g' = (\rho_p - \rho_f)g/\rho_p$, which accounts for buoyancy effects when an ambient fluid is present. The difference between ΔE_p and $\Delta E'_p$ may be considered as the energy transferred from particles to fluid due to the work done by buoyancy forces. Although we do not have an estimation of the work done by drag forces, it is expected to be negligible in the initial stage when the particle-fluid relative velocity remains small. The evolution of $\Delta E'_p$ is plotted in Fig. 12(b), which overlaps the initial evolution of E_k^p for 0.3 characteristic time (the square marker). Therefore, in this initial stage, particles do not consume energy, but only transfer energy to the surrounding fluid; the initial energy dissipation is purely owing to fluid viscosity. The zero-dissipation stage for particles shows that the underwater case is similar to its dry counterpart, as long as the buoyancy effect is accounted for (by g') and the drag force is not dominant, which reinforces our arguments in Figs. 6 and 7. Furthermore, when E_k^p starts to deviate from $\Delta E'_p$, it means that some extra energy is consumed by either particle-particle interactions or other forms of fluid-particle interaction (e.g., drag force).

The second row of Fig. 12 presents the evolution of partial kinetic energy for $a = 8$. In both dry and underwater cases, E_{ky}^p increases immediately towards a higher peak, while the development of E_{kx}^p is significantly delayed, with a lower peak. The delay corresponds to the initial free-fall stage, following which are the heap and spread stages where E_{kx}^p develops and vanishes, respectively (see also Fig. 3 for the three stages). Notably, E_{ky}^p vanishes much earlier than E_{kx}^p (see triangular markers), which is in contrast to the case when $a = 1$. This indicates that in the later stage only horizontal movements are present. Therefore, the distinct peaks of E_{kx}^p and E_{ky}^p clearly describe the three typical stages, i.e., collapse (before the first peak), heap (between peaks), and spread (after the second peak). In addition, in the underwater case, there is a lag between the kinetic energies of the fluid and particles, because the motion of the fluid is driven by particles. The peak of E_{kx}^f is higher than E_{ky}^f, as the horizontal motion of the fluid is more significant.

D. Energy dissipation: Effective coefficients of restitution

The different energy forms can help explain the scaling laws reported in Sec. IV C. In particular, the piecewise runout scaling in Fig. 8 can be linked to the energy evolution in the vertical and horizontal directions. Such an analysis has been reported in two-dimensional dry granular collapses [12]. Here, we analyze the energy dissipation and conversion in both dry and underwater situations.

The difference in energy dissipation (E_d) shown in Figs. 11 and 12 suggests that the conversion from potential to kinetic energy differs for tall and shallow columns. The conversion efficiency seems to depend on the initial aspect ratio a. Moreover, for tall columns, energy dissipation through particle interactions only starts when free-falling particles reach the bottom and then are redirected to the horizontal direction (Fig. 12), which indicates a different dependency on a for energy forms in different directions. Therefore, here we introduce two effective coefficients of restitution (ϵ_x and ϵ_y)

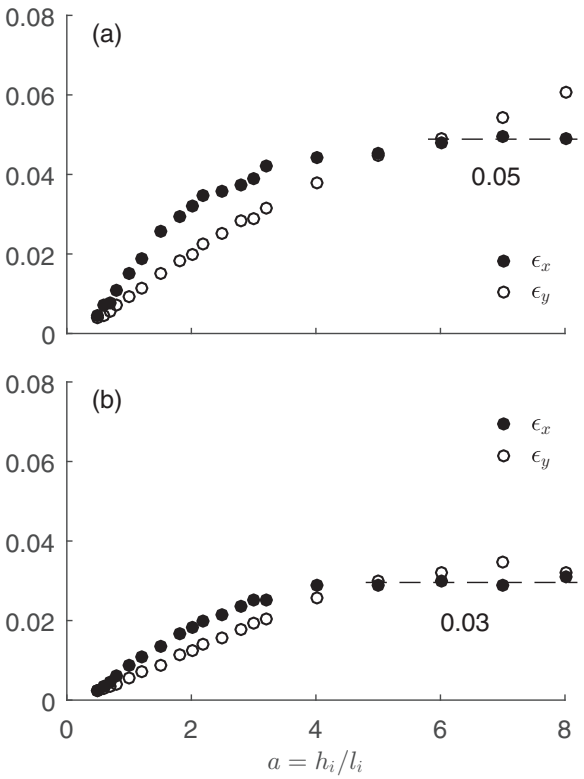

FIG. 13. Effective coefficients of restitution as a function of aspect ratio. (a) Dry. (b) Underwater.

to account for the energy loss in particles, respectively, in x and y directions. At any time t, we define

$$\epsilon_x = \frac{\langle E_{kx}^p \rangle}{E_0},\ \langle E_{kx}^p \rangle = \frac{1}{t}\int_0^t E_{kx}^p dt, \tag{10a}$$

$$\epsilon_y = \frac{\langle E_{ky}^p \rangle}{E_0},\ \langle E_{ky}^p \rangle = \frac{1}{t}\int_0^t E_{ky}^p dt, \tag{10b}$$

which gives an average picture of the energy dissipation over a given duration t. A higher value of ϵ_x or ϵ_y indicates less energy loss, thus a higher efficiency of conversion from potential to kinetic energy.

Figure 13 presents ϵ_x and ϵ_y over the whole flow duration as a function of a. In the dry case [Fig. 13(a)], ϵ_x increases with a and tends to saturate at around 0.05, while ϵ_y continues to increase with a. This result agrees with the previous study by Staron and Hinch [12]. The different trends of ϵ_x and ϵ_y may explain the change of slope in the runout scaling in Fig. 8. When a increases, more kinetic energy can be obtained in the vertical direction, following an exponential growth [12]. This is reasonable because a larger a means a higher initial potential energy. By contrast, the energy conversion in the horizontal direction does not increase infinitely with a; indeed, its increase slows down when $a > 2$ and saturates when $a = 6$, which is attributed to the fact that as the vertical momentum increases, the energy loss increases (due to harder impact) during the transition from vertical to horizontal movement, limiting the amount of momentum remained for particles to spread horizontally. As a result, the final runout distance l_f

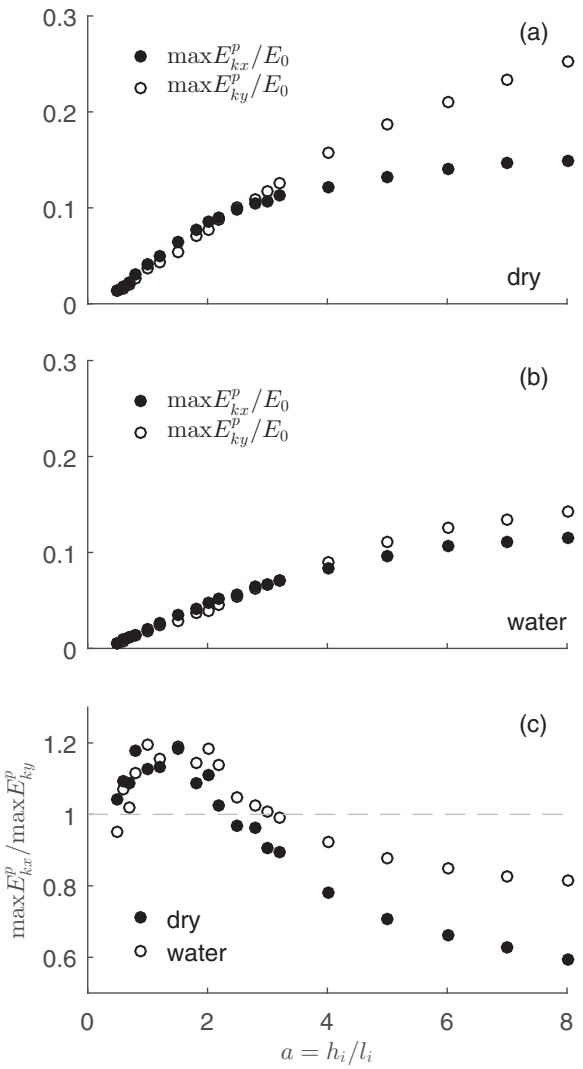

FIG. 14. Peak kinetic energy of particles as a function of aspect ratio. (a) Dry. (b) Underwater. (c) The ratio between peak kinetic energies in horizontal and vertical directions.

increases slower with a after a certain point (roughly, $a = 2.5$), leading to the piecewise runout scaling in Fig. 8.

The situation in the underwater case is similar [Fig. 13(b)]. In general, both ϵ_x and ϵ_y are lower in water than in air, which can be viewed as a damping effect from the ambient fluid that retards the involvement of vertical inertia. The upper limit of ϵ_x is 0.03 in water, lower than the value of 0.05 in air. However, the difference is not as significant as it appears in Fig. 12 when comparing the peaks of kinetic energy, probably due to the time averaging in the definition of ϵ_x that smears out the details of the unsteady collapse dynamics. In order to clearly characterize the effect of fluid in energy conversion, we further compare the peaks of E^p_{kx} and E^p_{ky} in the next subsection.

E. Energy conversion between vertical and horizontal directions

The dynamics of the unsteady collapse process may be better described by the peaks of E^p_{kx} and E^p_{ky}. Figure 14 presents $\max E^p_{kx}$ and $\max E^p_{ky}$ as a function of a. For dry cases [Fig. 14(a)], both peaks increase with a. When a remains small, $\max E^p_{kx}$ and $\max E^p_{ky}$ are similar, with the former being slightly higher, since the shallow columns tend to slide down and spread instantaneously. When a is greater than 2.5, the peak of E^p_{ky} overtakes E^p_{kx}, and the difference increases with a, which is due to the increasingly significant vertical inertia in the collapse stage of tall columns. Again, the crossover point $a = 2.5$ agrees with the transition of runout scaling in Fig. 8. For underwater cases [Fig. 14(b)], the overall trend is similar, and the crossing over occurs at around $a = 2$ and 3, agreeing with the smoother transition in Fig. 8. Both $\max E^p_{kx}$ and $\max E^p_{ky}$ are lower than those in dry cases. However, it is interesting to observe that the underwater cases exhibit a smaller difference between $\max E^p_{kx}$ and $\max E^p_{ky}$, compared to the dry cases. In other words, the energy conversion from vertical to horizontal directions seems to be more efficient in water especially for higher a. To quantify this efficiency, we show the ratio $\max E^p_{kx}/\max E^p_{ky}$ as a function of a [Fig. 14(c)].

As seen in Fig. 14(c), when a is small, the ratio $\max E^p_{kx}/\max E^p_{ky}$ is mainly greater than 1, and increases slightly with a. There is no clear trend differing dry and underwater cases. This is the fracturing regime (see Fig. 2) where the kinetic energy grows in both horizontal and vertical directions, with the former slightly more significant [see Figs. 11(a) and 11(b)]. For large values of a, at which distinct free-fall and spread stages emerge, the energy conversion from vertical fall to horizontal spread becomes clear [see Figs. 12(c) and 12(d)]. In this regime, $\max E^p_{kx}/\max E^p_{ky}$ is smaller than 1, which may be considered as the efficiency of energy conversion from vertical to horizontal directions. We observe from Fig. 14(c) that, for tall columns, the presence of an ambient fluid leads to more efficient energy conversions, which may compensate the difference between underwater and dry collapses; indeed, although the collapse dynamics in water differs significantly from the dry cases, the difference of runout distance between the two situations is not as large as expected (see Fig. 8). This finding is reminiscent of the fluid-inertia regime reported in [27], where immersed collapses may even run longer than the dry counterparts in some circumstances. Our explanation to this observation is threefold. First, in fluid, a lower vertical momentum is obtained during free fall, which leads to a softer impact on the bottom, thus dissipating less energy through particle collisions. This can be viewed as a "cushioning effect" of the fluid. Second, a thicker granular layer can be mobilized in water than in air, due to the "contact reducing" effect of interstitial fluids [27]. Indeed, by comparing Figs. 3(c) and 3(g), we observe that while the dry flow propagates with a higher *frontal* velocity, the velocity distribution is more uniform (and over a larger area) in the underwater flow. In other words, when immersed, the flow has a higher ability to utilize the available energy for horizontal spreading by putting more particles in motion. Finally, as particles spread horizontally, a considerable vortex structure develops in the flow direction, eroding the surface of the granular deposit and transporting particles further downstream (see Fig. 4), which alleviates the energy "loss" in particles that goes to the surrounding fluid.

VI. CONCLUDING REMARKS

In this paper, we perform coupled fluid-particle simulations to understand the dynamics and scaling laws of underwater granular collapses. The presence of fluid provides resistance to the flow of particles, leading to a shorter runout and thicker front. However, the influence of water becomes complicated for tall columns due to the interplay between particles and the ambient fluid. The eddies generated in water tend to propagate near the surface of the granular layer, which may carry sufficient inertia to erode the deposit surface.

In dry cases, we reproduce the power-law dependency of $(l_f - l_i)/l_i$ and h_f/l_i on a as reported in the literature. The exponent of the power law for tall columns matches with previous experimental measurements from a wide channel, highlighting the role of sidewalls in the granular collapse problem. The change of slope in the scaling law of $(l_f - l_i)/l_i$ occurs at around $a = 2.5$. In underwater cases, we find that the scaling law of $(l_f - l_i)/l_i$ tilts slightly downwards, with a smoother transition, while the dependency of h_f/l_i is more complicated under water; due to the fluid-inertial transport of particles, h_f/l_i drops significantly when $a \geqslant 4$, while the middle-region deposit thickness (h_f^m/l_i) increases accordingly.

The relevant length scales and timescales are explored in both dry and underwater situations. Using h_i and $\sqrt{h_i/g}$ (or $\sqrt{h_i/g'}$), we observe a roughly converged three-stage evolution (especially when $a \geqslant 1$), which includes an initial acceleration with a constant dimensionless acceleration of 0.75, a constant-velocity steady state, and a deceleration phase. The initial fall of tall columns is shown to be ballistic, with a dimensionless acceleration of 1. These results suggest that the reduced gravity $g' = (\rho_p - \rho_f)g/\rho_p$ is a proper scaling to account for the buoyancy effect when an ambient fluid is present. In fact, g' also applies to dry cases, where the density of fluid (air) is negligible.

To understand the effects of a on these scaling laws, we study in detail the energy conversion and dissipation. As a increases, we find an initial stage with negligible energy dissipation, showing that the upper part of a falling column does not interact significantly with its lower part during the free-fall stage, which may explain the nearly identical initial acceleration in the frontal region. The transition of the piecewise power-law relation between $(l_f - l_i)/l_i$ and a is also explained using energy arguments. With the increase of a, more initial potential energy is converted into kinetic energy in the vertical direction; however, the growth of horizontal energy slows down when $a > 2$ and saturates when $a > 4$, because more energy is dissipated when a tall column impacts on the bottom. The bifurcation of the growth rates in two directions occurs roughly at $a = 2.5$, leading to the change of slope in the runout scaling at the same point. Finally, we find that the presence of water increases the efficiency of energy conversion from vertical to horizontal directions by mobilizing more particles in the flow direction, thus compensating the reduction of runout distance in underwater cases.

This work focuses on a single type of ambient fluid, which is water. By varying fluid properties (viscosity and density), different flow regimes are expected to emerge [27,35,39]. On the basis of current findings, we will study the relevant scaling laws in different regimes in the future.

ACKNOWLEDGMENTS

The work was supported by Research Grants Council of Hong Kong (Grant No. 17203614) and FAP-DF, Brazil. This research was conducted in part using the research computing facilities and advisory services offered by Information Technology Services, The University of Hong Kong.

APPENDIX: NUMERICAL METHOD

In this Appendix, we present the governing equations (Appendix A 1) and the fluid-particle interaction model (Appendix A 2) for the CFD-DEM method.

1. Governing equations

In CFD we solve the local-averaged Navier-Stokes equations [40,41,49]

$$\frac{\partial}{\partial t}(\alpha_f \rho_f \mathbf{u}_f) + \nabla \cdot (\alpha_f \rho_f \mathbf{u}_f \mathbf{u}_f) = -\alpha_f \nabla p + \alpha_f \nabla \cdot \mathbf{T}_f + \alpha_f \rho_f \mathbf{g} - \mathbf{f}_{pf}, \quad \text{(A1a)}$$

$$\frac{\partial \alpha_f}{\partial t} + \nabla \cdot (\alpha_f \mathbf{u}_f) = 0, \quad \text{(A1b)}$$

where α_f is the volume fraction of fluid in each computational cell (i.e., porosity), $\mathbf{u}_f = (u_f, v_f, w_f)$ is the velocity vector of fluid, ρ_f is fluid density, p is pressure, $\mathbf{T}_f = \mu_f(\nabla \mathbf{u}_f + \nabla \mathbf{u}_f^{\mathrm{T}})$ is the extra-stress tensor of a fluid with viscosity μ_f, $\mathbf{f}_{pf}$ is the interaction force acting from the fluid phase to the particulate phase (given in the next subsection), and $\mathbf{g}$ is the gravitational acceleration vector.

In DEM, the motion of particles is governed by the Newton's second law [41]

$$m_i \frac{d\mathbf{u}_i}{dt} = \sum_{j=1}^{n_i^c} \mathbf{F}_{ij}^c + \mathbf{F}_i^f + m_i \mathbf{g}, \quad \text{(A2a)}$$

$$I_i \frac{d\boldsymbol{\omega}_i}{dt} = \sum_{j=1}^{n_i^c} \mathbf{M}_{ij}^c, \quad \text{(A2b)}$$

where $\mathbf{u}_i = (u_i, v_i, w_i)$ denotes the translational velocity of particle i, n_i^c is the number of contacts on particle i, $\mathbf{F}_{ij}^c$ is the contact force on particle i by particle j or a boundary, $\mathbf{F}_i^f$ is the particle-fluid interaction force acting on particle i, $\boldsymbol{\omega}_i$ is the particle angular velocity, I_i is the moment of inertia, and $\mathbf{M}_{ij}^c$ is the moment acting on particle i by particle j or a boundary.

The contact force $\mathbf{F}_{ij}^c$ is calculated using the Hertz model, which takes Young's modulus Y, Poisson's ratio ν, the coefficient of friction μ_p, and the coefficient of restitution e as input parameters (see [50] for details). The fluid force $\mathbf{F}_i^f$ includes buoyancy force $\mathbf{F}_i^b = V_i(-\nabla p + \nabla \cdot \mathbf{T}_f)$, where V_i is the volume of particle i, and drag force $\mathbf{F}_i^d$ (see later).

2. Fluid-particle interactions

The fluid-particle interaction is considered as a momentum exchange term in CFD,

$$\mathbf{f}_{pf} = K_{pf}(\mathbf{u}_f - \langle \mathbf{u}_p \rangle), \quad \text{(A3)}$$

where $\langle \mathbf{u}_p \rangle$ is the cell-based average particle velocity and K_{pf} is given by

$$K_{pf} = \frac{\sum_i F_i^d}{V_{fc}|\mathbf{u}_f - \langle \mathbf{u}_p \rangle|}, \tag{A4}$$

where V_{fc} is the volume of each computational fluid cell, and F_i^d is the magnitude of drag force acting on individual particles in DEM.

We calculate the drag force using the Di Felice model [51]

$$F_i^d = \tfrac{1}{8} C_d \rho_f \pi d_i^2 |\mathbf{u}_f - \mathbf{u}_i| \alpha_f^{1-\chi}, \tag{A5}$$

where d_i is the diameter of particle i, C_d is drag coefficient, and χ is a corrective coefficient. Both C_d and χ are a function of the particle Reynolds number Re_p:

$$C_d = \left(0.63 + \frac{4.8}{\sqrt{\mathrm{Re}_p}}\right)^2, \tag{A6a}$$

$$\chi = 3.7 - 0.65 \exp\left[-\frac{(1.5 - \log_{10}\mathrm{Re}_p)^2}{2}\right] \tag{A6b}$$

with

$$\mathrm{Re}_p = \frac{\alpha_f \rho_f d_i |\mathbf{u}_f - \mathbf{u}_i|}{\mu_f}. \tag{A7}$$

[1] R. Delannay, A. Valance, A. Mangeney, O. Roche, and P. Richard, J. Phys. D: Appl. Phys. **50**, 053001 (2017).
[2] S. Utili, T. Zhao, and G. Houlsby, Eng. Geol. **186**, 3 (2015).
[3] F. Løvholt, S. Bondevik, J. S. Laberg, J. Kim, and N. Boylan, Geophys. Res. Lett. **44**, 8463 (2017).
[4] O. Roche, M. Attali, A. Mangeney, and A. Lucas, Earth Planet. Sci. Lett. **311**, 375 (2011).
[5] M. Farin, A. Mangeney, and O. Roche, J. Geophys. Res.: Earth Surf. **119**, 504 (2014).
[6] Z. Lai, L. E. Vallejo, W. Zhou, G. Ma, J. M. Espitia, B. Caicedo, and X. Chang, Geophys. Res. Lett. **44**, 12181 (2017).
[7] E. Lajeunesse, A. Mangeney-Castelnau, and J. P. Vilotte, Phys. Fluids **16**, 2371 (2004).
[8] E. Lajeunesse, J. B. Monnier, and G. M. Homsy, Phys. Fluids **17**, 103302 (2005).
[9] G. Lube, H. E. Huppert, R. S. J. Sparks, and M. A. Hallworth, J. Fluid Mech. **508**, 175 (2004).
[10] G. Lube, H. E. Huppert, R. S. J. Sparks, and A. Freundt, Phys. Rev. E **72**, 041301 (2005).
[11] N. J. Balmforth and R. R. Kerswell, J. Fluid Mech. **538**, 399 (2005).
[12] L. Staron and E. J. Hinch, J. Fluid Mech. **545**, 1 (2005).
[13] R. Zenit, Phys. Fluids **17**, 031703 (2005).
[14] L. Staron and E. J. Hinch, Granular Matter **9**, 205 (2007).
[15] L. Girolami, V. Hergault, G. Vinay, and A. Wachs, Granular Matter **14**, 381 (2012).
[16] L. Lacaze and R. R. Kerswell, Phys. Rev. Lett. **102**, 108305 (2009).
[17] R. R. Kerswell, Phys. Fluids **17**, 057101 (2005).
[18] A. Mangeney-Castelnau, F. Bouchut, J. P. Vilotte, E. Lajeunesse, A. Aubertin, and M. Pirulli, J. Geophys. Res.: Solid Earth **110**, B09103 (2005).
[19] E. Larrieu, L. Staron, and E. J. Hinch, J. Fluid Mech. **554**, 259 (2006).
[20] E. E. Doyle, H. E. Huppert, G. Lube, H. M. Mader, and R. S. J. Sparks, Phys. Fluids **19**, 106601 (2007).
[21] P.-Y. Lagrée, L. Staron, and S. Popinet, J. Fluid Mech. **686**, 378 (2011).
[22] I. R. Ionescu, A. Mangeney, F. Bouchut, and O. Roche, J. Non-Newtonian Fluid Mech. **219**, 1 (2015).
[23] C.-H. Lee, Z. Huang, and Y.-M. Chiew, Phys. Fluids **27**, 113303 (2015).
[24] E. J. Fern and K. Soga, Acta Geotechnica **11**, 659 (2016).
[25] C. Lusso, A. Ern, F. Bouchut, A. Mangeney, M. Farin, and O. Roche, J. Comput. Phys. **333**, 387 (2017).
[26] L. Rondon, O. Pouliquen, and P. Aussillous, Phys. Fluids **23**, 073301 (2011).
[27] V. Topin, Y. Monerie, F. Perales, and F. Radjaï, Phys. Rev. Lett. **109**, 188001 (2012).
[28] A. Bougouin and L. Lacaze, Phys. Rev. Fluids **3**, 064305 (2018).
[29] R. M. Iverson, M. E. Reid, N. R. Iverson, R. G. LaHusen, M. Logan, J. E. Mann, and D. L. Brien, Science **290**, 513 (2000).
[30] M. Pailha, M. Nicolas, and O. Pouliquen, Phys. Fluids **20**, 111701 (2008).
[31] P. Mutabaruka, J.-Y. Delenne, K. Soga, and F. Radjai, Phys. Rev. E **89**, 052203 (2014).
[32] C.-H. Lee and Z. Huang, Adv. Water Resour. **115** 286 (2017).
[33] C. Wang, Y. Wang, C. Peng, and X. Meng, Phys. Fluids **29**, 103307 (2017).
[34] P. Si, H. Shi, and X. Yu, Phys. Fluids **30**, 083302 (2018).
[35] C. Cassar, M. Nicolas, and O. Pouliquen, Phys. Fluids **17**, 103301 (2005).
[36] C. Meruane, A. Tamburrino, and O. Roche, J. Fluid Mech. **648**, 381 (2010).
[37] C. Meruane, A. Tamburrino, and O. Roche, Phys. Rev. E **86**, 026311 (2012).
[38] A. Bougouin, L. Lacaze, and T. Bonometti, J. Fluid Mech. **826**, 918 (2017).
[39] S. Courrech du Pont, P. Gondret, B. Perrin, and M. Rabaud, Phys. Rev. Lett. **90**, 044301 (2003).
[40] Y. Tsuji, T. Kawaguchi, and T. Tanaka, Powder Technol. **77**, 79 (1993).
[41] C. Kloss, C. Goniva, A. Hager, S. Amberger, and S. Pirker, Prog. Comput. Fluid Dyn. **12**, 140 (2012).
[42] OPENCFD, OPENFOAM: the Open Source Computational Fluid Dynamics (CFD) Toolbox.
[43] L. Jing, C. Y. Kwok, Y. F. Leung, and Y. D. Sobral, Int. J. Numer. Anal. Methods Geomech. **40**, 62 (2016).
[44] J. Zhao and T. Shan, Powder Technol. **239**, 248 (2013).
[45] T. Zhao, F. Dai, and N.-w. Xu, Landslides **14**, 189 (2017).

[46] J. Koivisto, M. Korhonen, M. J. Alava, C. P. Ortiz, D. Durian, and A. Puisto, Soft Matter **13** 7657 (2017).
[47] L. Jing, C. Y. Kwok, Y. F. Leung, and Y. D. Sobral, Phys. Rev. E **94**, 052901 (2016).
[48] A. Lorenz, C. Tuozzolo, and M. Y. Louge, Exp. Mech. **37**, 292 (1997).
[49] T. B. Anderson and R. Jackson, Ind. Eng. Chem. Fundam. **6**, 527 (1967).
[50] L. E. Silbert, D. Ertaş, G. S. Grest, T. C. Halsey, D. Levine, and S. J. Plimpton, Phys. Rev. E **64**, 051302 (2001).
[51] R. Di Felice, Int. J. Multiphase Flow **20**, 153 (1994).